catalysts

MDPI

Article

Mixed-Metal Semiconductor Anodes for Electrochemical Water Splitting and Reactive Chlorine Species Generation: Implications for Electrochemical Wastewater Treatment

Su Young Ryu and Michael R. Hoffmann *

Linde Center for Global Environmental Science, Division of Engineering & Applied Science, Linde-Robinson Laboratory, California Institute of Technology, Pasadena, CA 91125-0001, USA; syryu@caltech.edu

* Correspondence: mrh@caltech.edu; Tel.: +1-626-395-4391

Academic Editors: Bunsho Ohtani and Jae Sung Lee

Received: 16 February 2016; Accepted: 31 March 2016; Published: 20 April 2016

Abstract: A procedure for the preparation of semiconductor anodes using mixed-metal oxides bound together and protected with a TiO_2 nanoglue has been developed and tested in terms of the relative efficiencies of the oxygen evolution (OER), the reactive chlorine species evolution (RCS), and the hydrogen evolution (HER) reactions. The composition of the first anode is a Ti metal substrate coated with $IrTaO_x$ and overcoated with TiO_2 (P_{25}) that was mixed with TiO_2 nanogel, while the second anode consists of a Ti metal substrate coated with $IrTaO_x$ and an over-coating layer of La-doped sodium tantalate, $NaTaO_3$:La. The experimental efficiencies for water splitting ranged from 62.4% to 67.5% for H_2 evolution and 40.6% to 60.0% for O_2 evolution. The corresponding over-potentials for the Ti/IrTa-TiO_2 and Ti/IrTa-$NaTaO_3$:La anodes coupled with stainless steel cathodes of the same dimensions were determined to be 437 mV and 367 mV for the OER, respectively, and 239 mV and 205 mV for RCS, respectively. The preparation procedure described herein should allow for easier production of large-surface area anodes at lower costs than standard methods.

Keywords: a facile methodology for electrode fabrication; catalysts; water splitting; wastewater treatment

1. Introduction

We have recently developed prototype electrochemical reactor systems for the treatment of human or domestic wastewater that are powered by either AC or DC power sources [1–4]. In these electrochemical treatment systems, human wastewater is oxidized at an array of semiconductor anodes based on the generation rate of Reactive Chlorine Species (RCS), which is a key active compound in the process of wastewater treatment. Water oxidation and Cl^- oxidation to free chlorine (Cl_2) have been known to compete against each other during electrocatalysis due to sharing the active sites for both processes, while H_2 is produced at matched metal cathodes. Hydrogen generation via electrochemical water splitting is generally environmental friendly and reliable for the large-scale hydrogen production that would be required for a hydrogen economy [5–7]. The cathodic generation of molecular hydrogen is effectively limited by the corresponding anodic oxidation of water. In order to improve the efficiency of water splitting, it is essential to reduce the anodic overpotential for the oxygen evolution reaction (OER) by using optimized electron transfer catalysts. If a chloride ion is present in the electrolyte or wastewater undergoing treatment, then the oxidation of Cl^- to Cl_2 takes place at lower applied potentials in light of the overpotential for the OER [4].

A significant effort combining both theoretical and experimental work has been made over the past decade in order to identify new materials that could lower the overpotential of the OER [8]. RuO_2

and IrO_2 base anodes are referred to as dimensionally stable anodes (DSA), which are often used both for the electrochemical generation of reactive chlorine species (RCS) and the OER at relatively low overpotentials [9]. However, the high cost of the iridium oxide precursor reagents coupled with the relatively poor long-term stability of IrO_2 has essentially impeded the large-scale commercial application of DSAs.

The process of attachment of nanoparticulate metal oxide semiconductors (e.g., IrO_2, RuO_2, Ta_2O_5, SnO_2, Bi_2O_3) to base-metal surfaces is critical for producing efficient anodes and, in some cases, functionalized cathodes. Anatase (TiO_2) nanogels have been reported to be a sticky inter-particle binding agent or nanoglue that results in improved electrochemical performance and higher current efficiencies for base-metal supported semiconductor anodes [10].

2. Results and Discussion

2.1. Anode Characterization

The sequentially layered anode assembly can be visualized in a series of SEM micrographs showing the surface morphologies as determined by EDS analyses for each layer in Figure 1. The surface sampling depth was 1–2 µm for the determination of the elemental composition. The SEM micrograph of the mixed-metal oxide layer of IrO_2/Ta_2O_5 on the Ti base-metal plate has a wave-like surface morphology in contrast to the typically observed cracked-film morphology for IrO_2 deposits applied to base-metal substrates [11]. The initially deposited layer consists of Ir, O, Ti, and Ta, while the seal coating layer made from $Ni(NO_3)_3{\cdot}6H_2O$ contains NiO with minor amounts of $Ni(OH)_2$ as determined by XPS analysis. The electron probe microanalysis of the Ti-IrTa-$NaTaO_3$:La composite anode shows that the outermost surface of the anode consists of $NaTaO_3$:La mixed with nanoparticulate TiO_2 in distinctly different size domains (Figure 2). The magnified SEM image shown in Figure 2d allows us to distinguish the location of TiO_2 nanoparticles that are located between the larger $NaTaO_3$:La particles. The TiO_2 nanoglue serves as an inter-particle binding agent via interlocking surface-hydroxyl groups of hydrated TiO_2 with the surface hydroxyl groups of hydrated $NaTaO_3$. These interlocking surface hydroxyl groups condense during elevated temperature dehydration to form > M–O–M < bonds during the annealing steps at 100 °C [10].

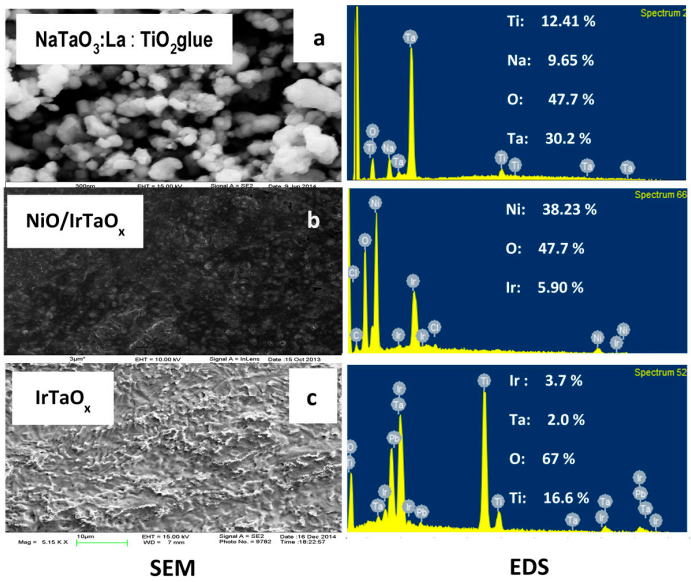

Figure 1. SEM micrographs and associated EDS data with the associated chemical composition for the sequential coating layers. (**a**) Top surface over-coating layer (**b**) Second coating layer of NiO applied as an optional layer, containing a minor amount of $Ni(OH)_2$ as determined by XPS analysis. (**c**) Primary coating of $IrTaO_x$ on the surface of the Ti base-metal support.

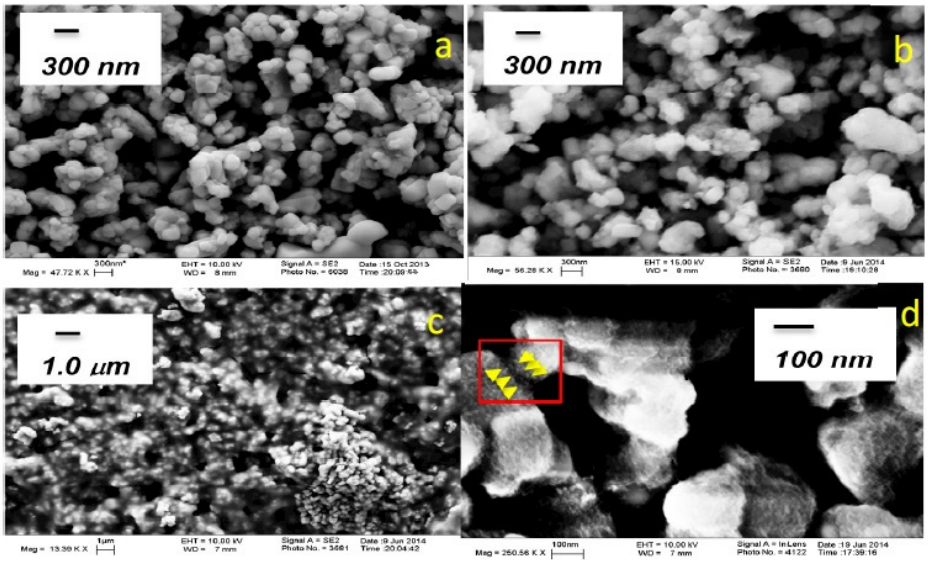

Figure 2. SEM images of overcoated substrate surfaces coupled together with TiO_2 nanogel: (**a**) $NaTaO_3$; (**b**) $NaTaO_3$:La mixed with 1.5% TiO_2 nanogel; (**c**) additional TiO_2 nanogel applied on the surface shown in Figure 2b for a total of 3 wt. % TiO_2 nanogel; (**d**) higher resolution SEM image of the over-coating layer of $NaTaO_3$:La mixed with 1.5% TiO_2 nanogel inter-particle binding agent that highlights a nanogel binder location shown in the red box.

The FTIR spectra shown in the Figure 3 can be used to compare the combination of $NaTaO_3$:La and TiO_2 (P_{25}) in the particle phase (Figure 3a) to the electrode surface when prepared with TiO_2 nanoglue as shown in Figure 3b. The IR spectrum of the TiO_2 nanoglue composite is dominated by surface hydroxyl groups that are characterized by a strong > OH stretch centered near 3100 cm^{-1}. A broader peak normally observed at 535 cm^{-1} that is characteristic of skeletal > Ti–O–Ti < vibrations was not detected in the dehydrated TiO_2 nanoparticles. Peaks at 1400 and 1500 cm^{-1} are attributed to C–O vibrational modes that originate from either residual titanium isopropoxide or from acetic acid, which was added to adjust pH. The TiO_2 nanogel was used during the formation of the electrode outer layers of the Ti-IrTa-TiO_2 and Ti-IrTa-$NaTaO_3$:La electrodes in order to facilitate the inter-particle binding of TiO_2 (P_{25}) and $NaTaO_3$:La; however, the nanoglue was still detectable after annealing as measured by the OH-vibrational peak at 3100 cm^{-1}. The XRD pattern of Ti-IrTa-$NaTaO_3$:La is consistent with a combination of anatase TiO_2 that originated from amorphous TiO_2 nanoglue and $NaTaO_3$:La. In contrast, a mixed phase of anatase and rutile TiO_2 is evident in the XRD pattern for Ti-IrTa-TiO_2 (Figure 3b).

SEM micrographs clearly show a nanostepped surface morphology of $NaTaO_3$:La due to a change of the surface structure of $NaTaO_3$ due to doping with lanthanum, while the surface of un-doped $NaTaO_3$ appears to be relatively flat (Figure S1) [12]. NiO deposited on to $NaTaO_3$ doped with La has been reported to be an efficient water-splitting photocatalyst. The evolution of O_2 is reported to take place on the grooves of the nanostep, while H_2 is catalytically evolved on the ultrafine NiO particles. The loading of NiO nanoparticle coupled with the doping of La into the structure of $NaTaO_3$ increases the lifetime of the trapped electrons and holes, which lead to higher yields of H_2 and O_2 under continuous illumination [12].

Given the favorable photosynthetic water-splitting properties of $NaTaO_3$:La upon irradiation, we decided to utilize it for the outer layer of our metal oxide semiconductor anode. The synthesized TiO_2 nanogel is characterized by various analytical techniques: TEM image of TiO_2 nanoglue indicated around 8 nm of the particle size; XRD pattern confirmed an anatase phase of crystalline structure;surface hydroxyl groups were verified by FTIR; and the band-gap energy for the nanoglue was determined to be 3.13 eV (Figure S2).

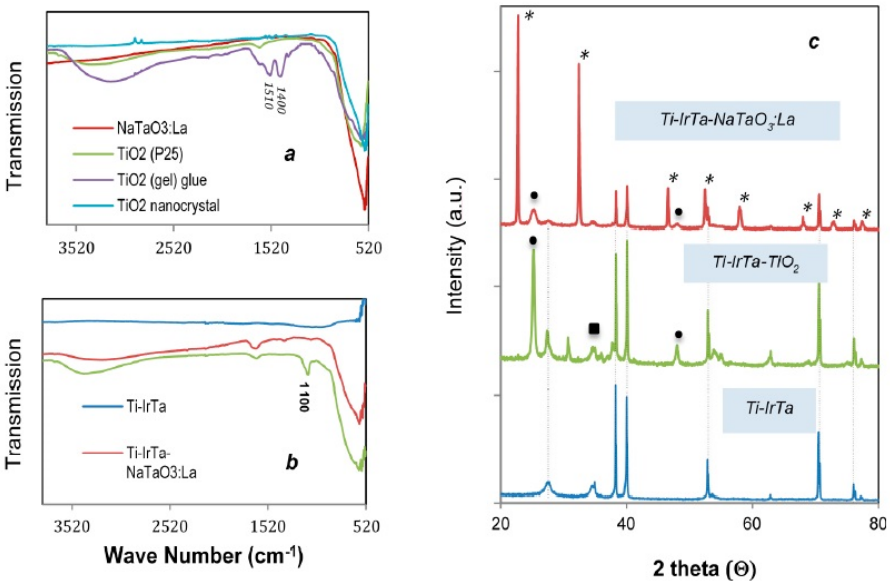

Figure 3. (**a**) FTIR spectra of the metal oxide powders used for fabrication of anode, TiO_2 (P_{25}), $NaTaO_3$:La, TiO_2 nanogel, and TiO_2 nanocrystals. (**b**) FTIR spectra of the Ti-IrTa, Ti-IrTa-TiO_2, Ti-IrTaTi-IrTa-$NaTaO_3$:La anodes. (**c**) XRD spectra of Ti-IrTa-$NaTaO_3$:La, Ti-IrTa-TiO_2 and Ti-IrTa electrode. Ti-IrTa electrode pattern was dominated by the Ti foil XRD pattern due to the thin layer of of $IrTaO_x$. XRD pattern of $NaTaO_3$:La (*), an anatase phase of TiO_2 nanogel (●), and a rutile phase from TiO_2 (P_{25}) (■).

2.2. Electrochemical Characterization

The mixed metal oxide anodes were characterized by cyclic voltammetry (CV). The anodes were paired with stainless steel (SS) cathodes that were separated by 5 mm. The CV measurements were carried out in either a 50 mM NaCl or a 50 mM K_2SO_4 solution at a fixed scanning rate of 20 mV s^{-1} over a range of applied potentials ranging from 0 to 2.0 V. In Figure 4, the resulting CV plots are shown for (a) IrO_2/Ta_2O_5 coated on to a Ti base-metal plate (designated as Ti-IrTa), (b) a sealing coat of NiO on Ti-IrTa (designated as Ti-IrTa-Ni), (c) an over-coating layer of TiO_2 on Ti-IrTa (designated as Ti-IrTa-TiO_2), and (d) an over-coating layer of $NaTaO_3$:La on Ti-IrTa (designated as Ti-IrTa-$NaTaO_3$). The Reactive Chlorine Species (RCS) and oxygen onset potentials (OER) were determined from the intersection of the tangents between the baseline and the current signals. The observed onset potentials occurred close to 1.2 V for the production of RCS and 1.25 V for the evolution of oxygen, OER. The corresponding overpotential for the RCS was determined to be 239 mV for the Ti-IrTa-TiO_2 anode and 205 mV for Ti-IrTa-$NaTaO_3$:La anode, respectively (Figure 4c).

The CV profiles observed in the 50 mM K_2SO_4 electrolyte solutions had steeper polarization curves compared to the comparative measurement in NaCl solutions except for the NiO-coated electrode (Figure 4b). The CV curves obtained in the K_2SO_4 electrode solutions indicate that only the OER is taking place. In this case, the overpotentials observed for the OER on Ti-$IrTaO_x$-TiO_2 and on Ti-$IrTaO_x$-$NaTaO_3$:La were determined to be 437 mV and 367 mV, respectively. The measured overpotentials are comparable to previously reported values for IrO_2 of 300 mV [13]. The anode with a sealing coat of NiO on the Ti-$IrTaO_x$ electrode had a relatively gentle J–V curve (*i.e.*, slope) and a lower overpotential of 212 mV. This may be attributed to surface corrosion during electrochemical water oxidation [9]. In comparison, anodes prepared with an outer layer of $NaTaO_3$:La and TiO_2 (P_{25}) bound together with TiO_2 nanoglue had steeper J–V curves with a cathodic shift in the onset potential for both electrolyte solutions that was close to 100 mV.

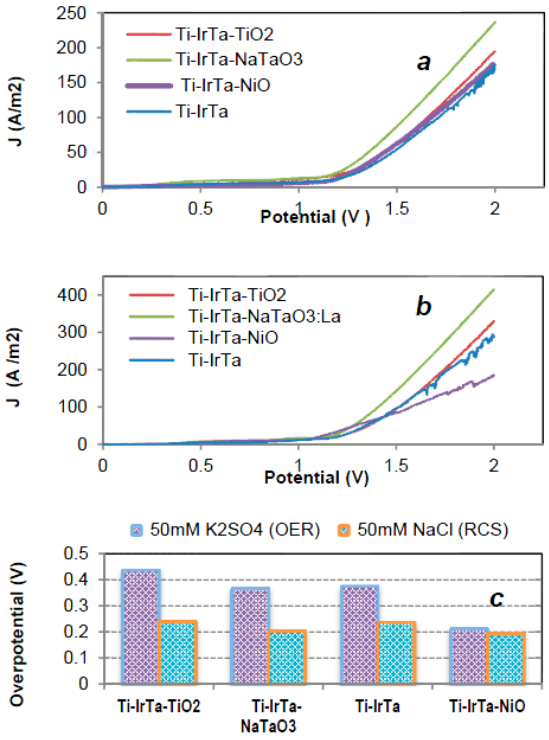

Figure 4. Cyclic voltammetry (CV) results for IrO_2/Ta_2O_5 pre-coated anodes (Ti-IrTa), TiO_2 over-coated anodes (Ti-IrTa-TiO_2), and $NaTaO_3$:La over-coated on $IrO_2Ta_2O_5$ (Ti-IrTa-$NaTaO_3$:La). (**a**) CV in a 50 mM NaCl solution; (**b**) CV in a 50 mM K_2SO_4 solution; and (**c**) the estimated overpotential obtained.

2.3. Electrocatalysis

Given the current level of interest in photo-electrochemical water splitting, chlorine production, and electrochemical wastewater treatment [14–16] for small scale application or for distributed water treatment systems, alternatives to the platinum group metals or boron-doped diamond electrodes are needed to lower the costs of electrochemical treatment [17–26]. Alternative electroactive materials are needed in order to lower the cost of production of semiconductor anodes for larger-scale practical applications. A major limitation of DSA systems that are currently in use is the dependence on the use of IrO_2 or RuO_2 as primary ohmic contact material. For example, the typical precursor reagents used, $IrCl_3$ and $RuCl_3$, are quite expensive with the cost of $IrCl_3$ at three times the cost of $RuCl_3$.

Zaradjanin *et al.* [27] reported on the critical importance of the chemical composition of the semiconductor anode materials in terms of improving interfacial electron transfer rates and for optimization of electrochemical efficiencies. In the case of reactions taking place in an NaCl electrolyte, there is major competition between the OER and RCS reactions for the same active sites on the anode surfaces [18,28].

2.3.1. Water Oxidation

Metal oxide semiconductor electrodes are often used for electrochemical water splitting into O_2 and H_2 in alkaline, acidic, or neutral solutions in spite of their relatively large bandgap energies coupled with valence band edges close to −3.0 eV. The half-reactions for water splitting and corresponding overall reaction are given in Equations (1)–(3):

$$2\,H_2O \rightarrow O_2 + 4\,H^+ + 4\,e^- \,(E = 1.23\,V_{NHE} - 0.059V/pH) \quad (1)$$

$$4\,H^+ + 4\,e^- \rightarrow 2H_2 \,(E = 0\,V_{NHE} - 0.059V/pH) \quad (2)$$

$$2\,H_2O \rightarrow O_2 + 2\,H_2 \quad (3)$$

The Ti-IrTa-TiO_2 and Ti-IrTa-$NaTaO_3$:La anodes were tested for their water splitting capability in 50 mM K_2SO_4 alone to avoid a direct composition of reactive chlorine species (RCS) from chloride at the electrode surfaces. The OER reaction mechanism on the metal oxide anodes can be considered to take place according to the sequence of reactions outlined by Comninellis [29]. The key reactions in the sulfate electrolyte solutions involve surface bound hydroxyl groups, >MOH, bound or adsorbed water >MOH_2^+, or a hydroxide ion within the near surface electrical double layer, which depends on the electrolyte solution pH and the pH_{zpc} of the active metal oxide at the solid–solution interface [17,30].

$$MO_x + H_2O \rightarrow MO_x(OH) + H^+ + e^- \quad (4)$$

$$MO_x(OH) \rightarrow MO_{(x+1)} + H^+ + e^- \quad (5)$$

$$MO_x(OH) \rightarrow MO_x + \tfrac{1}{2}O_2 + H^+ + e^- \quad (6)$$

$$MO_{(x+1)} \rightarrow MO_x + \tfrac{1}{2}O_2 \quad (7)$$

If the applied potential in a sulfate electrolyte solution is kept below +2.0 V, then the oxidation of SO_4^{2-} to SO_4^- and $S_2O_8^{2-}$ should not be a competitive process. Figure 4b shows the cyclic voltammetry (CV) profile of the anodes, Ti-IrTa-TiO_2 and Ti-IrTa-$NaTaO_3$:La, in a 50 mM K_2SO_4 electrolyte solution at the circum-neutral pH of 5.8. The Gibbs free energy (ΔG) for water splitting at room temperature is 237.16 kJ/mol at a potential of 1.23 V at pH 0. The observed onset potential for the Ti-IrTa-$NaTaO_3$ anode coupled with stainless steel cathode is about 1.255 V, which is giving an overpotential of 367 mV at circum-neutral pH in 50 mM K_2SO_4. The rate of H_2 and O_2 generation was determined for the Ti-IrTa-$NaTaO_3$ and Ti-IrTa-TiO_2 anodes using 6 cm^2 active surfaces coupled with stainless steel cathodes at a separation distance of 5 mm as a function of the applied anodic potential, which varied from 1.35 to 2.0 V. Figure 5 shows the time-dependent evolution of H_2 and O_2 as a function of time as measured simultaneously, and O_2 generation rate and current density, which increases with an increase in applied potential. The measured mole ratio of evolved H_2 to O_2 was not found to be 2 to 1 while the generation rate of H_2 and O_2 decreased as a function of time. The less than 2 to 1 stoichiometric ratio in the reactor headspace may be due to a number of factors including different gas solubility between O_2 and H_2 in water, which depends on the relative partial pressures in headspace of the reactor. The O_2 solubility is 25 times that of H_2 at 25 °C and a total pressure of 1.0 atm. In a well-mixed reactor that is lacking a salt bridge or proton-exchange membrane separator, oxygen can be simultaneous oxidized and reduced. Figure 6 shows the H_2 and O_2 evolution rates along with the current densities and current efficiencies. The generation rates of H_2 and O_2 were found to increase linearly with an increase in current density, as given in Table 1. The faradaic efficiencies ranged from 62.4% to 67.5% for H_2 and from 40.6% to 60% for O_2, respectively. At these efficiencies the Ti-IrTa-TiO_2 and Ti-IrTa-$NaTaO_3$ anodes, if coupled with more efficient cathodes, could be used for H_2 generation [31].

Table 1. H_2 evolution rates and current efficiencies as a function of the applied anodic potential over the range from 1.375 to 2.0 V during electrolysis of water in 50 mM K_2SO_4.

Electrode	Potential (V *vs.* NHE)	Current (mA)	Current Density (A/m^2)	H_2 Evolution ($mol/h \cdot m^2$)	O_2 Evolution ($mol/h \cdot m^2$)	Current Efficiency (%) for H_2/O_2
Ti-IrTa-TiO_2	1.38	43	71.7	0.834	-	62.4/-
	1.5	72	120	1.392	0.680	62.2/60
	1.75	131	218.3	2.64	-	64.8/-
	2.0	210	350	4.404	-	67.5/-
Ti-IrTa-$NaTaO_3$	1.38	41	68.3	-	0.258	-/40.6
	1.5	91	151.7	1.8	0.678	62/48
	1.75	149	248.3	-	1.326	-/57.2
	1.9	213	355	-	1.715	-/51.8

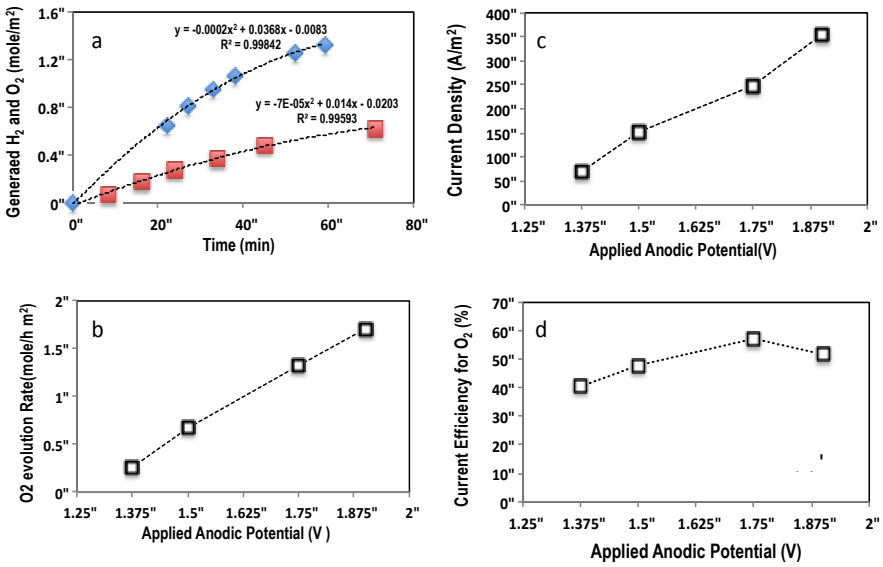

Figure 5. The generation rates for H_2 and O_2 were determined using 6 cm^2 active surface areas for specific test anode and cathode. The Ti-IrTa-$NaTaO_3$ anode was paired with a stainless steel cathode at a separation distance of 5 mm. Evolution rates were measured as a function of the applied anodic potential over the range of 1.35 to 2.0 V *vs.* SHE in a 50 mM K_2SO_4 electrolyte:(**a**) evolved H_2 and O_2 as measured simultaneously as a function of time at the 1.5 applied anodic potential; (**b**) O_2 evolution rate; and (**c**) current density as function of applied potential; with (**d**) current efficiency for O_2 evolution.

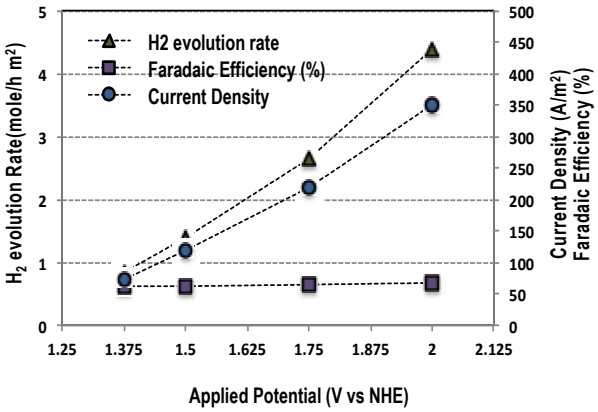

Figure 6. H_2 evolution rates and associated faradaic efficiencies (HER) and current densities as a function of applied potential using the Ti-IrTa-TiO_2 anodes (6 cm^2) coupled with stainless steel cathodes with an electrode separation distance of 5 mm in a 50 mM K_2SO_4 electrolyte solution.

2.3.2. Wastewater Treatment

There is a growing interest in the use of electrochemistry for wastewater treatment, especially in smaller-scale distributed systems. The oxidation of organic and reduced inorganic compounds on the surface of metal oxides anodes is initiated via the formation of surficial hydroxyl radicals and/or by direct electron transfer to surface-trapped holes [17,30]. Chloride ions (Cl^-), which are normally present at variable levels in wastewater, undergo "indirect" oxidation by surface-bound hydroxyl radicals, leading to the production of reactive chlorine species (RCS) including free chlorine (Cl_2, HOCl, ClO^-) [17,30] and chlorine radicals (Cl^-, Cl_2^-) [2,16]. The RCS generation rate increases with an increase in applied voltage (E_a) up to a limiting value. The Ti-IrTa-TiO_2 and Ti-IrTa-$NaTaO_3$:La anodes were evaluated with respect to their free chlorine generation rates and electrochemical efficiencies when coupled with matched stainless steel cathodes. Figure 7 shows the observed generation rates

for the RCS, current densities, and current efficiencies as a function of applied anodic potential over the range of +1.35 to +2.5 V during potentiostatic electrolysis (Table 2). The production of RCS is directly proportional to the electrode current density. The OER and RCS have similar standard redox potentials of 1.23 and 1.36 V at pH 0, respectively. On the surface of the mixed-metal oxide anodes, RCS evolution appears to be kinetically favored even though the OER is thermodynamically favored. The electrochemical oxidation of Cl^- on metal oxide anodes can be attributed to either oxidation by hydroxyl radical or by active lattice oxygens [17,32,33] as illustrated below:

$$MO_x(OH) + Cl^- \rightarrow MO_x + Cl + OH^- \quad (8)$$

where $k_8 = 4.3 \times 10^9\ M^{-1}\ s^{-1}$ for the homogeneous oxidation of Cl^- by OH.

$$MO_{(x+1)} + Cl^- \rightarrow MO_x + ClO^- \quad (9)$$

In typical wastewater with relatively high chloride ion concentrations, there is an obvious competition between the RCS production and the OER on the anode surfaces.

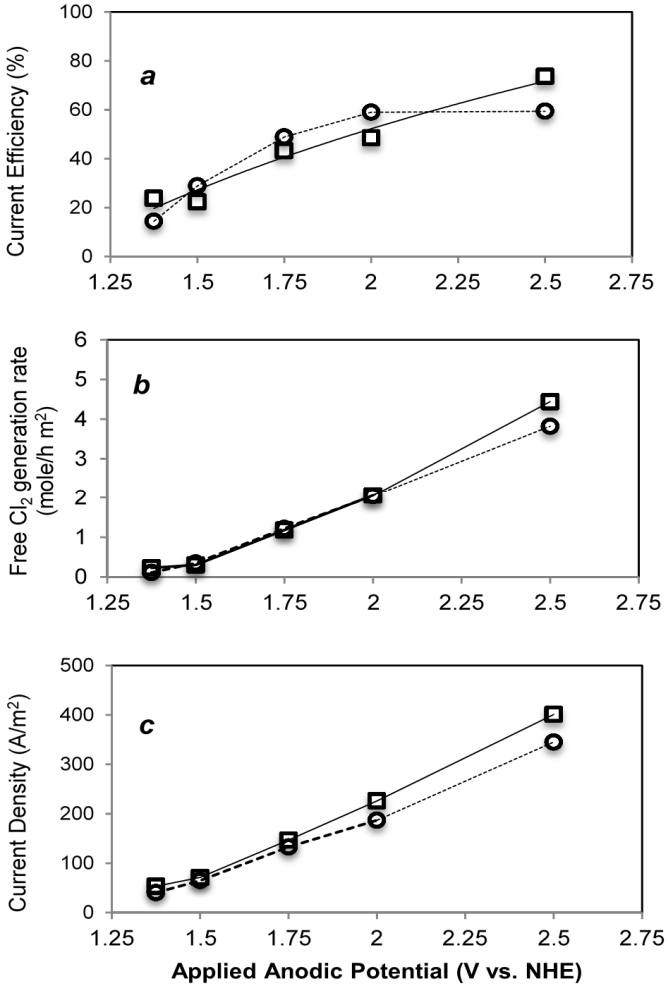

Figure 7. Comparative performance of the Ti-IrTa-TiO_2 (○) and Ti-IrTa-$NaTaO_3$:La (▫) anodes coupled with stainless steel cathodes in terms of (**a**) current efficiency, (**b**) reactive chlorine generation rates, and (**c**) current density as a function of applied anodic potential during potentiostatic electrolysis of 50 mM NaCl solutions using the same cell dimensions and surface areas.

Table 2. Measured rates of reactive chlorine generation, current efficiencies, and current densities as a function of applied anodic potential from 1.38 to 2.5 V NHE during potentiostatic electrolysis in 50 mM NaCl solutions.

Electrode (Anode)	Potential (V *vs.* NHE)	Current (mA)	Current Density (A/m^2)	Free Cl_2 Evolution ($mol/h \cdot m^2$)	Current Efficiency (%)
$Ti\text{-}IrTa\text{-}TiO_2$	1.38V	24.2	40.3	0.11	16.4
	1.5 V	38.8	64.7	0.35	31.3
	1.75 V	79.7	132.8	1.22	48.9
	2.0 V	112	186.7	2.05	59
	2.5 V	207	345	3.82	59.4
$Ti\text{-}IrTa\text{-}NaTaO_3$	1.3 V	32	53.3	0.23	23.8
	1.5 V	42.6	71	0.30	22.3
	1.75 V	88	146.7	1.18	43.25
	2.0 V	135.6	226	2.06	48.5
	2.5 V	241	401	4.44	73.7

In the case of RuO_2 or RuO_2/TiO_2 the MO_{x+1} surficial sites appear to be the principal reactive sites for chloride oxidation [34]. In a typical sequence it initiates by an oxidation of Cl^- to a surface bound OCl^- (Equation (10)), the generation of reactive chlorine species (RCS) is developed as first order in concentration of Cl^- with a pseudo-steady-state approximation on $MO_x(OCl^-)$. However, at circumneutral pH, the Cl_2 reacts with water to form hypochlorous acid and hypochlorite, as described in Equations (14) and (11). The formation of chlorate, $ClO_3{}^-$, which we expect to detect from a subsequent reaction that is led by OCl^- or HOCl as a primary reductant(Equations (15) and (16)). The stepwise sequence of reactions for the production of RCS can be written as follows:

$$MO_{(x+1)} + Cl^- \rightarrow MO_{(x)} + OCl^- \quad (10)$$

$$H^+ + {}^-OCl \rightleftharpoons HOCl \; (pK_{aHOCl} = 7.53) \quad (11)$$

$$MO_x(OH) + Cl^- \rightarrow MO_x + Cl + OH^- \quad (12)$$

$$2Cl \rightleftharpoons Cl_2 \quad (13)$$

$$Cl_2 + H_2O \rightarrow HOCl + Cl^- + H^+ \quad (14)$$

$$2MO_{(x+1)} + ClO^- \rightarrow 2MO_x + ClO_3{}^- \quad (15)$$

$$2MO_{(x+1)} + HOCl \rightarrow 2MO_x + ClO_3{}^- + H^+ \quad (16)$$

2.3.3. Urea Degradation

Urea is the most abundant nitrogen-containing compound in freshly discharged human waste. Upon hydrolysis, urea forms NH_3 and CO_2, eventually leading to the formation of chloramines, $NHCl_2$, NH_2Cl, and NCl_3. Urea decomposition and subsequent chlorination using mixed metal oxide anodes [35–37] has been reported. Urea degradation using the alternative $Ti\text{-}IrTa\text{-}TiO_2$ and $Ti\text{-}IrTa\text{-}NaTaO_3$:La anodes has been investigated as part of this study. During electrochemical oxidation, N_2 and CO_2 along with H_2 and O_2 were formed as gaseous products, while $NH_4{}^+$, $NO_3{}^-$, NH_2Cl, $NHCl_2$, and NCl_3 were formed as reactive intermediates and products in the liquid phase. Simultaneous analysis of the gas and liquid phases was performed with a quadrupole mass spectrometer (QMS) for the headspace gas analysis and a DX-2000 ion chromatographic system was used to quantify ions in the aqueous phase [3]. Free reactive chlorine (HOCl or OCl^-, Figure 7) is a primary oxidant during urea degradation at relatively fast reaction rates. Figure 8 shows the concentration vs. time profiles of $NH_4{}^+$ and NO_3 formed during potentiostatic electrolysis at an applied voltage of 2.25 V of a solution of urea at an initial concentration of 41.6 mM with an electrolyte concentration of 50 mM Cl^- in a reaction volume of 70 mL. During a typical reaction, the free molecular chlorine (Cl_2) was below the detection limit, while the majority of total chlorine was found to be RCS plus an array of inorganic chloramines [38]. The observed concentration vs. time profiles of aqueous

products are similar to previous reports [3,38]. This suggests that urea degradation takes place via reactions between urea and electrochemically-generated reactive chlorine (*i.e.*, RCS) rather than by a direct oxidation pathway on the electrode surface, which normally takes place via direct electron transfer from nitrogen in urea to the active sites on the anode surface [1]. The first step during the oxidation of urea by chlorine has been reported to proceed slowly and thus it is the rate-determining step in the overall electrochemical oxidation and degradation of urea [38–40]. Based on previously reported results, RCS are formed on the anode surface, which then leads to formation of urea chlorinate to tetrachloro-urea that is subsequently oxidized to CO_2 along with the formation of chloramines. The reaction sequence shown below in Equations (17) to (26) has been proposed to account for the decomposition of urea during chlorination:

$$2\,(H_2N)_2CO + (OCl^-/HOCl/Cl^-) \rightarrow H_2N(CO)NHCl + H_2N(CO)NCl_2 + 2\,H_2O \quad (17)$$

$$Cl_2N(CO)NCl_2 + H_2O \rightarrow CO_2 + 2\,NHCl_2 \quad (18)$$

$$H_2N(CO)NHCl + HOCl \rightarrow CO_2 + 2\,NH_2Cl \quad (19)$$

$$H_2N(CO)NHCl + H_2O \rightarrow NH_2Cl + NH_2(CO)OH \quad (20)$$

$$NH_2(CO)OH + Cl^- \rightarrow ClHN(CO)OH + HOCl \rightarrow CO_2 + NHCl_2 + H_2O \quad (21)$$

$$NH_2Cl + H_2O \rightarrow NH_4^+ + OCl^- \quad (22)$$

$$NH_2Cl + HOCl \rightarrow NHCl_2 + H_2O \quad (23)$$

$$NHCl_2 + HOCl \rightarrow NCl_3 + H_2O \quad (24)$$

$$NCl_3 + HOCl + 2H_2O \rightarrow NO_3^- + 4Cl^- + 5H^+ \quad (25)$$

$$NHCl_2 + NH_2Cl \rightarrow N_2 + 3Cl^- + 3H^+ \quad (26)$$

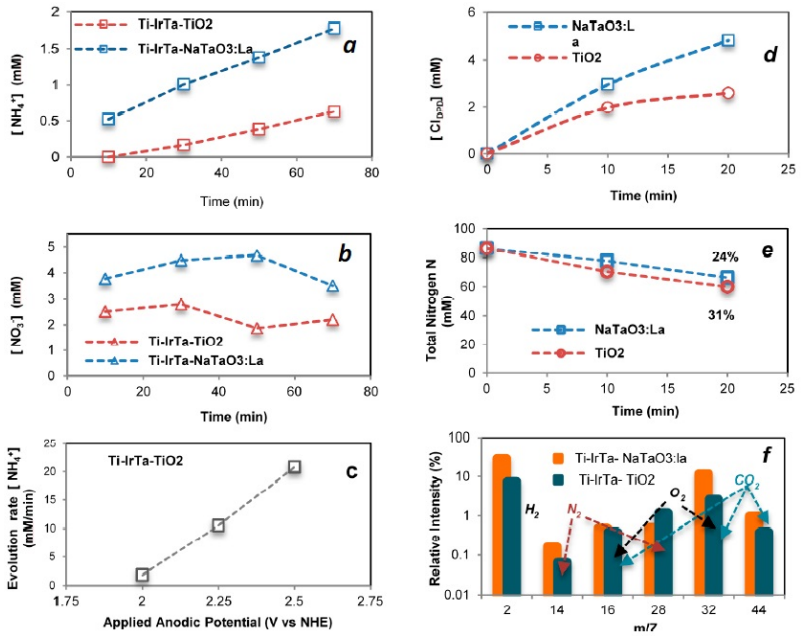

Figure 8. (**a**) [NH_4^+] and (**b**) [NO_3^-] *versus* time during the potentiostatic electrolysis of a solution containing 42 mM of urea and 50 mM NaCl in a volume of 70 mL for the Ti-IrTa-TiO_2 and Ti-IrTa-$NaTaO_3$:La anodes; (**c**) NH_4^+ production rate as a function of applied potential; (**d**) total chlorine production (Cl_{DPD}) at +2.25 V for Ti-IrTa-TiO_2 and Ti-IrTa-$NaTaO_3$:La; (**e**) $[\Sigma N]_T$ *vs.* time; (**f**) head-space gas composition at an anodic potential of +3.25 V as determined by online MS.

The reversible hydrolysis of chloramines generates NH_4^+/NH_3 depending on pH and the [RCS] [39]. Trichloramine oxidation by RCS also leads to NO_3^- formation [1,38]; however, the yields are quite low for the electrochemical oxidation of urea initiated by RCS. The observed time profiles ofNH_4^+ and NO_3^- shown in Figure 8a,b are consistent with previous reports for urea degradation on a bismuth-doped TiO_2 electrode (BiO_x/TiO_2); in addition, the NH_4^+ ion in liquid phase increased proportionally along with an increased applied anodic potential, as shown in Figure 8c. The total nitrogen decay profile could be used as a surrogate for urea decomposition, since TN in the aqueous phase includes [NO_3^-], [NH_4^+], [NH_xCl_{3-x}], although some of the chloramines react to form N_2, as illustrated above via breakpoint chlorination. In general, the summation of the detected concentration of NH_4^+ and NO_3^-, and Cl_{DPD}-containing nitrogen in the form of a chloramine (NH_xCl_{3-x}), is much smaller than the degassed N_2, N_2O, NO, or NO_2.

The TN removal rate, in the case of the Ti-IrTa-TiO_2 anode, was 31% after 20 min of electrolysis at an applied potential of 3.25 V. This level of reduction is higher than we had previously reported for a multi-metal anode with an overcoat of Bi-doped TiO_2[2]. The rate of urea degradation based on the TN decay was ~1.0 mM min^{-1} with the Ti-IrTa-$NaTaO_3$:La anode. In comparison, the rate of urea degradation or decomposition was found to be 1.3 times faster with the Ti-IrTa-TiO_2 anode than with the Ti-IrTa-$NaTaO_3$:La anode. The time profiles for the generated N_2 and CO_2 during electrolysis of urea degradation are shown in Figure S3. From the time-dependent concentration profiles of Figure 8, it is clear that the [NH_4^+] increased slowly compared to nitrate. NCl_3, which is a likely intermediate leading to the formation of NO_3^- via the reaction of NH_2Cl and free chlorine (HOCl) [38], was at pH 6.5. On the other hand, NH_4^+ might be formed through a reversible hydrolysis of the inorganic chloramine (NH_2Cl). The formation of CO_2 is generated via a different pathway from N_2 generation, as described in Equations (18) and (19) above, and it is indicated that the CO_2 formation is slower than the N_2 generation, as shown in the time profiles of Figure S3.

3. Experimental Details

3.1. Synthetic Procedures: La-Doped $NaTaO_3$ and TiO_2 Nanogel

Lanthanum-doped $NaTaO_3$ powder (denoted as $NaTaO_3$:La) was prepared in a solid-state reaction [11] Reagent grade starting materials, La_2O_3, Na_2CO_3, and Ta_2O_5, were mixed in a ratio Na:La:Ta = $(1 - x$ to x to 1). An excess amount of sodium (5 mol%) was added to the mixture in order to compensate for the volatilization during thermal processing. The reagent mixture was calcined in air at 1170 K for 1 h and 1420 K for 10 h with periodic breaks for grinding. Excess sodium was removed by water extraction after calcination. On average, the doping level was 2 mol% La into $NaTaO_3$. TiO_2 was synthesized according to a procedure used by Li *et al.* [10]. Titanium tetra-isopropoxide, $Ti(OCH(CH_3)_2)_4$ or (TTIP), was diluted with 2-propanol and then added drop by drop into Milli-Q water where the mass ratio was M_{H2O}/M_{TTIP} = 110 in the presence of acetic acid at pH = 2. After complete hydrolysis the suspension was heated at 90 °C for 4 h with vigorous stirring. TiO_2 particles were collected by centrifugation to yield a concentrated 15 wt. % gel. The resulting 15 wt. % TiO_2 nanogel is defined as a "nanoglue."

3.2. Electrode Fabrication

The metal oxide hetero-junction anodes were prepared by sequential deposition as follows: Ti metal coupons (2×5 cm^2) were pretreated by sand blasting the surface; the sand-blasted Ti-metal coupons were then etched in a boiling 10 wt. % oxalic acid solution for 10 min. The first deposition layer of $IrTaO_x$ (*i.e.*, anti-passivation ohmic contact) was prepared by coating with the precursor solution that contained 73 mM H_2IrCl_6 with 27 mM $TaCl_5$ dissolved in a solution of ethanol and isopropanol at a 1:1 volume ratio. The deposited layer of $IrTaO_x$ was then annealed for 10 min at 525 °C. This procedure was repeated four to six times; the final over-coating layer was annealed for an additional hour at 525 °C. A protective over-coating layer of TiO_2 in the form of a viscous paste was then applied. The

alcohol-TiO_2 coating paste was prepared by mixing 10% by weight Aeroxide P_{25} TiO_2 with 15 wt. % of the TiO_2 nanogel; the mixture was then ultrasonically mixed with a 20 kHz sonication system for 1 h. The weight ratio of the P_{25} TiO_2 to the nanogel TiO_2 was fixed at a ratio of 7:1. The $NaTaO_3$:La overcoat was then prepared as a slurry by mixing 15 wt. % $NaTaO_3$:La suspended in alcohol also containing 15 wt. % TiO_2 nanogel at a weight ratio of 3.75:1. The outer-layer slurry coating was then applied with a doctor blade using tape as a spacer on the IrTaO*x* layer. The sequential deposition process can be summarized in the following steps used for the preparation of anode "A." (1) A mixed suspension of IrO_2/Ta_2O_5 at the mole ratio of 73:27 is deposited to provide an anti-passivation layer; (2) a protective sealing coat of $Ni(NO_3)_3{\cdot}6H_2O$ is then applied; and (3) a slurry of $TiO_2(P_{25})$ and TiO_2 nanogel is deposited at the weight ratio of 3.75:1. The preparation of anode "B" was prepared following a two-step sequence of (1) application of an initial coating on the Ti base-metal with a mixture of IrO_2/Ta_2O_5 at the mole ratio of 73:27 and then (2) deposition of a suspension slurry of $NaTaO_3$:La and TiO_2 nanogel at the weight ratio of 2.85:1. The preparation sequence involves depositing an initial ohmic contact layer on to the base Ti metal, which is followed by a sealing coat layer that is then followed by an overcoating layer (or an overcoat). After each coating layer is deposited, the composite material is thermally annealed as described above.

The electrochemical setup consisted of a mixed-metal oxide semiconductor anode coupled with a stainless steel cathode a separation distance of 5 mm. The effective surface areas for both anodes and cathodes were 6 cm^2 (3 cm × 2 cm). The temperature-controlled electrochemical cells were connected to a potentiostat (SP-50, Bio-Logic, Grenoble, France). The applied anodic potential, *Ea*, was adjusted based on continuous monitoring of the response current (*I*) and cathodic potential (*Ec*). Electrochemical water splitting was carried out in electrolyte solutions of either 50 mM NaCl or 50 mM K_2SO_4 in a cell with total volume of 105 mL; this volume included 35 mL of head space was used to measure the production of H_2 and O_2 during electrolysis. Before each experiment, the reactor was purged high purity N_2 for 45 min. The anodic and cathodic current efficiencies (Faradaic Efficiency, *FE*) for the production free reactive Cl_2 (e.g., Cl_2, HOCl, and OCl^-) and/or O_2 and H_2 were determined according to the expression *FE* (%) = [Cl_2 production rate (mol/s) × n × F/I] × 100, in which "n" is the number of electrons transferred for the production of Cl_2, O_2, and H_2, respectively, I is the current (A), t is time (s) and F is the Faraday constant (96,485 C/mol). The free reactive chlorine concentrations were determined using a HACH standard DPD (*N*,*N*-diethyl-p-phenylenediamine) method and a HACH DR 900 colorimeter (HACH, Loveland, CO, USA). The method was calibrated using a SpecCheck Secondary Gel Standard Set for DPD Chlorine that has an analytical range from 0 to 6.5 mg/L as free reactive Cl_2.

3.3. Instrumentations

X-ray photoelectron spectroscopy (XPS) analysis was conducted by using a surface science instrument M-probe spectrometer with a monochromatic 1486.6 eV Al Kα X-ray line source directed 35° to the sample surface, which is controlled by ESCA25 capture software. UV-Vis diffuse reflectance spectrum was measured using a Shimadzu UV-2101PC (dual beam) (Shimadzu, Kyoto, Japan) equipped with an integration sphere attachment (Shimadzu ISR-260, Shimadzu, Kyoto, Japan), which is used for reflection and transmittance measurement of liquid and solids. IR spectra were obtained using a Nicolet iS50 FTIR spectrometer (Thermo Scientific Inc., Waltham, MA, USA) integrated a diamond accessory. XRD apparatus used is a PANalytical X-ray diffractometer (X'Pert Pro) (PANalytical, Westborough, UK) which is a closed system that is completely remote controlled via computer. The XRD data was obtained by automatic scanning of a given range of the angle, 20° to 80°. SEM images were collected using a ZEISS 1550VP Field Emission Scanning Electron Microscope (SEM) (Carl Zeiss, Jena, Germany) operating at 10 kV acceleration voltages. Elemental analysis was performed using an energy dispersive X-ray spectroscopy system (EDS, Carl Zeiss, Jena, Germany) integrated with SEM, with the electron beam voltage set at 15 KeV. The particle size of TiO_2 nanogel was estimated with a Transmission Electron Microscope (TEM) image. The analysis of the interest ions, NO_3^- and NH_4^+,

were quantified by Dionex ICS2000 ion chromatography system. The amount of H_2 and O_2 evolved during water splitting electrolysis was analyzed using gas chromatography (HP 5890 Series II, Hewlett Packard, Palo Alto, CA, USA) with a thermal conductivity detector (TCD). Helium was used as the carrier gas for O_2 detection, while nitrogen was used as carrier for H_2 detection, and the separation was achieved with a molecular sieve column (30 m × 0.32 mm × 12.00 μm).

4. Conclusions

The alternative anode formulations, Ti-IrTa-TiO_2 and Ti-IrTa-$NaTaO_3$:La, had overpotentials of 437 mV and 239 mV, respectively, for OER with Faradaic efficiencies ranging from 62.4% to 67.5% for H_2 and 40.6% to 60.0% for O_2. The Faradaic efficiencies for RCS evolution were as high as 73.7% depending on the applied potential. The overpotentials were determined to be 239 mV and 205 mVfor RCSE, respectively. It appears that the relatively high efficiencies for electrolysis may be due to the use of a TiO_2 nanogel as an inter-particle binding agent and electron relay.

Supplementary Materials: Figure S1: SEM and EDS of $NaTaO_3$:La shows a nanostep surface morphology (A), while the surface of nondoped $NaTaO_3$ was flat (B), caused by a change of the structure of $NaTaO_3$ with the dope of lanthanum, Figure S2: TEM image that determined particle size as around 8 nm, and XRD patterns that revealed the anatase structural phase of TiO_2 and confirmed abundant surface hydroxyl group in FTIR spectrum. The bandgap was determined as 3.13 eV at its UV-vis reflectance spectrum, Figure S3: Time profile for the generated N_2 and CO_2 gas during electrolysis of urea degradation: (a) a time profile of an estimated N_2 and CO_2 gas generation; (b) a time profile of head-space gas composition for the major gases, H_2, O_2, N_2, and CO_2.

Acknowledgments: This study is supported by Bill & Melinda Gates Foundation (BMGF RTTC Grant No. 1105724). The authors are grateful to Byung-Kuk Yoo (Caltech) for his support for TEM measurement.

Author Contributions: Su Young Ryu performed the experiments and data analysis and she wrote the initial draft of the paper. Michael Hoffmann was the principal investigator of the project; he edited the draft manuscript for publication.

Conflicts of Interest: The authors declare no conflict of interest.

References

1. Cho, K.; Hoffmann, M.R. Urea degradation by electrochemically generated reactive chlorine species: Products and reaction pathways. *Environ. Sci. Technol.* **2014**, *48*, 11504–11511. [CrossRef] [PubMed]
2. Cho, K.; Kwon, D.; Hoffmann, M.R. Electrochemical treatment of human waste coupled with molecular hydrogen production. *RSC Adv.* **2014**, *4*, 4596–4608. [CrossRef]
3. Cho, K.; Qu, Y.; Kwon, D.; Zhang, H.; Cid, C.A.; Aryanfar, A.; Hoffmann, M.R. Effects of anodic potential and chloride ion on overall reactivity in electrochemical reactors designed for solar-powered wastewater treatment. *Environ. Sci. Technol.* **2014**, *48*, 2377–2384. [CrossRef] [PubMed]
4. Cho, K.; Hoffmann, M.R. $Bi_xTi_{1-x}O_z$ functionalized heterojunction anode with an enhanced reactive chlorine generation efficiency in dilute aqueous solutions. *Chem. Mater.* **2015**, *27*, 2224–2233. [CrossRef]
5. Zeng, K.; Zhang, D.K. Recent progress in alkaline water electrolysis for hydrogen production and applications. *Prog. Energy Combust. Sci.* **2010**, *36*, 307–326. [CrossRef]
6. Tributsch, H. Photovoltaic hydrogen generation. *Int. J. Hydrog. Energy* **2008**, *33*, 5911–5930. [CrossRef]
7. Hall, D.E. $Ni(OH)_2$ impregnated anodes for alkaline water electrolysis. *J. Electrochem. Soc.* **1983**, *130*, 317–321. [CrossRef]
8. Doyle, R.L.; Godwin, I.J.; Brandon, M.P.; Lyons, M.E. Redox and electrochemical water splitting catalytic properties of hydrated metal oxide modified electrodes. *Phys. Chem. Chem. Phys. PCCP* **2013**, *15*, 13737–13783. [CrossRef] [PubMed]
9. McCrory, C.C.; Jung, S.; Peters, J.C.; Jaramillo, T.F. Benchmarking heterogeneous electrocatalysts for the oxygen evolution reaction. *J. Am. Chem. Soc.* **2013**, *135*, 16977–16987. [CrossRef] [PubMed]
10. Li, Y.; Lee, W.; Lee, D.K.; Kim, K.; Park, N.G.; Ko, M.J. Pure anatase TiO_2 "nanoglue": An inorganic binding agent to improve nanoparticle interconnections in the low-temperature sintering of dye-sensitized solar cells. *Appl. Phys. Lett.* **2011**, *98*, 103301. [CrossRef]

11. Lyons, M.E.; Floquet, S. Mechanism of oxygen reactions at porous oxide electrodes. Part 2-oxygen evolution at RuO_2, IrO_2 and $Ir_xRu_{1-x}O_2$ electrodes in aqueous acid and alkaline solution. *Phys. Chem. Chem. Phys. PCCP* **2011**, *13*, 5314–5335. [CrossRef] [PubMed]
12. Kato, H.; Asakura, K.; Kudo, A. Highly efficient water splitting into H_2 and O_2 over lanthanum-doped $NaTaO_3$ photocatalysts with high crystallinity and surface nanostructure. *J. Am. Chem. Soc.* **2003**, *125*, 3082–3089. [CrossRef] [PubMed]
13. Kotz, R.; Stucki, S. Stabilization of RuO_2 by IrO_2 for anodic oxygen evolution in acid media. *Electrochem. Acta* **1986**, *31*, 1311–1316. [CrossRef]
14. Park, H.; Vecitis, C.D.; Choi, W.; Weres, O.; Hoffmann, M.R. Solar-powered production of molecular hydrogen from water. *J. Phys. Chem. C* **2008**, *112*, 885–889. [CrossRef]
15. Park, H.; Vecitis, C.D.; Hoffmann, M.R. Solar-powered electrochemical oxidation of organic compounds coupled with the cathodic production of molecular hydrogen. *J. Phys. Chem. A* **2008**, *112*, 7616–7626. [CrossRef] [PubMed]
16. Park, H.; Vecitis, C.D.; Hoffmann, M.R. Electrochemical water splitting coupled with organic compound oxidation: The role of active chlorine species. *J. Phys. Chem. C* **2009**, *113*, 7935–7945. [CrossRef]
17. Martinez-Huitle, C.A.; Ferro, S. Electrochemical oxidation of organic pollutants for the wastewater treatment: direct and indirect processes. *Chem. Soc. Rev.* **2006**, *35*, 1324–1340. [CrossRef] [PubMed]
18. Martinez-Huitle, C.A.; Brillas, E. Decontamination of wastewaters containing synthetic organic dyes by electrochemical methods: A general review. *Appl. Catal. B Environ.* **2009**, *87*, 105–145. [CrossRef]
19. Raut, A.S.; Cunningham, G.B.; Parker, C.B.; Klem, E.J.D.; Stoner, B.R.; Deshusses, M.A.; Glass, J.T. Disinfection of *E. coli* contaminated urine using boron-doped diamond electrodes. *J. Electrochem. Soc.* **2014**, *161*, G81–G81. [CrossRef]
20. Antonin, V.S.; Santos, M.C.; Garcia-Segura, S.; Brillas, E. Electrochemical incineration of the antibiotic ciprofloxacin in sulfate medium and synthetic urine matrix. *Water Res.* **2015**, *83*, 31–41. [CrossRef] [PubMed]
21. Marmanis, D.; Dermentzis, K.; Christoforidis, A.; Ouzounis, K.; Moumtzakis, A. Electrochemical treatment of actual dye house effluents using electrocoagulation process directly powered by photovoltaic energy. *Desalin. Water Treat.* **2015**, *56*, 2988–2993. [CrossRef]
22. Muazu, N.D.; Jarrah, N.; Bukhari, A. Kinetic modeling of electrochemical oxidation of phenol on boron-doped diamond anode in the presence of some inorganic species. *Desalin. Water Treat.* **2015**, *56*, 3005–3012. [CrossRef]
23. Radjenovic, J.; Sedlak, D.L. Challenges and opportunities for electrochemical processes as next generation technologies for the treatment of contaminated water. *Environ. Sci. Technol.* **2015**, *49*, 11292–11302. [CrossRef] [PubMed]
24. Zollig, H.; Fritzsche, C.; Morgenroth, E.; Udert, K.M. Direct electrochemical oxidation of ammonia on graphite as a treatment option for stored source-separated urine. *Water Res.* **2015**, *69*, 284–294. [CrossRef] [PubMed]
25. Zollig, H.; Morgenroth, E.; Udert, K.M. Inhibition of direct electrolytic ammonia oxidation due to a change in local pH. *Electrochim. Acta* **2015**, *165*, 348–355. [CrossRef]
26. Zollig, H.; Remmele, A.; Fritzsche, C.; Morgenroth, E.; Udert, K.M. Formation of chlorination byproducts and their emission pathways in chlorine mediated electro-oxidation of urine on active and nonactive type anodes. *Environ. Sci. Technol.* **2015**, *49*, 11062–11069. [CrossRef] [PubMed]
27. Zeradjanin, A.R.; Menzel, N.; Schuhmann, W.; Strasser, P. On the faradaic selectivity and the role of surface inhomogeneity during the chlorine evolution reaction on ternary Ti-Ru-Ir mixed metal oxide electrocatalysts. *Phys. Chem. Chem. Phys.* **2014**, *16*, 13741–13747. [CrossRef] [PubMed]
28. Exner, K.S.; Anton, J.; Jacob, T.; Over, H. Chlorine evolution reaction on RuO_2(110): *Ab initio* atomistic thermodynamics study-Pourbaix diagrams. *Electrochim. Acta* **2014**, *120*, 460–466. [CrossRef]
29. Comninellis, C. Electocatalysis in the electrochemical conversion/combustion of organic pollutants for waste water treatment. *Electrochem. Acta* **1994**, *39*, 1857–1862. [CrossRef]
30. Panizza, M.; Cerisola, G. Direct and mediated anodic oxidation of organic pollutants. *Chem. Rev.* **2009**, *109*, 6541–6569. [CrossRef] [PubMed]
31. Cheng, S.; Logan, B.E. Sustainable and efficient biohydrogen production via electrohydrogenesis. *PNAS* **2007**, *104*, 18871–18873. [CrossRef] [PubMed]

32. Hansen, H.A.; Man, I.C.; Studt, F.; Abild-Pedersen, F.; Bligaard, T.; Rossmeisl, J. Electochemical chlorine evolution at rutile oxide (110) surfaces. *Phys. Chem. Chem. Phys.* **2010**, *12*, 283–290. [CrossRef] [PubMed]
33. Trasatti, S. Progress in the understanding of the mechanism of chlorine evolution at oxide electrodes. *Electrochem. Acta* **1987**, *32*, 369–382. [CrossRef]
34. Krishtalik, L.I. Kinetics and mechanism of anodic chlorine and oxygen evolution reactions on transition metal oxide electrodes. *Electrochem. Acta* **1981**, *26*, 329–337. [CrossRef]
35. Simka, W.; Piotrowski, J.; Robak, A.; Nawrat, G. Electrochemical treatment of aqueous solutions containing urea. *J. Appl. Electrochem.* **2009**, *39*, 1137–1143. [CrossRef]
36. Hernlem, B.J. Electrolytic destruction of urea in dilute chloride solution using DSA electrodes in a recycled batch cell. *Water Res.* **2005**, *39*, 2245–2252. [CrossRef] [PubMed]
37. Carlesi Jara, C.; di Giulio, S.; Fino, D.; Spinelli, P. Combined direct and indirect electroxidation of urea containing water. *J. Appl. Electrochem.* **2008**, *38*, 915–922. [CrossRef]
38. Blatchley, E.R.; Cheng, M.M. Reaction mechanism for chlorination of urea. *Environ. Sci. Technol.* **2010**, *44*, 8529–8534. [CrossRef] [PubMed]
39. Jafvert, C.T.; Valentine, R.L. Reaction scheme for the chlorination of ammoniacal water. *Environ. Sci. Technol.* **1992**, *26*, 577–586. [CrossRef]
40. Deborde, M.; von Gunten, U. Reactions of chlorine with inorganic and organic compounds during water treatment-Kinetics and mechanisms: A critical review. *Water Res.* **2008**, *42*, 13–51. [CrossRef] [PubMed]